# Electron density determination in the divertor volume of ASDEX Upgrade via Stark broadening of the Balmer lines

**S. Potzel, R. Dux, H.W. Müller, A. Scarabosio, M. Wischmeier and ASDEX Upgrade team**

Max-Planck-Institut für Plasmaphysik, EURATOM Association, Boltzmannstraße 2, 85748 Garching, Germany

E-mail: Steffen.Potzel@ipp.mpg.de

**Abstract.** In this article we present the development of a new diagnostic capable of determining the electron density in the divertor volume of ASDEX Upgrade. It is based on the spectroscopic measurement of the Stark broadening of the Balmer lines. In this work two approaches of calculating the Stark broadening, i.e. the unified theory and the model microfield method, are compared. It will be shown that both approaches yield similar results in the case of Balmer lines with high upper principal quantum numbers $n$. In addition, for typical ASDEX Upgrade parameters the influence of the Zeeman splitting on the high $n$ Balmer lines is found to be negligible. Moreover, an assumption for the Doppler broadening of $T_n = 5\,\mathrm{eV}$, which is the maximum Frank-Condon dissociation energy of recycled neutrals, is sufficient. The initial electron density measurements performed using this method are found to be consistent with both Langmuir probe and pressure gauge data.

## 1. Introduction

In ASDEX Upgrade (AUG) Langmuir probes are commonly used to measure the electron density, $n_e$, in the divertor. This is a local measurement of $n_e$ in front of the divertor target. In AUG, no diagnostic is available to provide information about $n_e$ away from the target in the divertor volume. This information, however, is especially in detached divertor regimes of high interest. To address this issue, a new spectroscopic method using the Stark broadening of the Balmer lines has been developed to determine $n_e$ in the divertor volume of AUG.

Instead of determining the FWHM of a Stark broadened Balmer line via a fit of a Voigt function [1, 2] and comparing it to tabulated values [3], we fit entire theoretical Stark profiles to the measured Balmer line to deduce the electron density. To this end, two different theories calculating the Stark broadening are compared, i.e. the unified theory and the model microfield method. In addition, the unified theory is used to investigate the influence of the magnetic field on the line shapes by including an

additional Zeeman splitting. Finally, the effect of the neutral temperature via Doppler broadening is also examined.

This paper is structured as follows: In section 2 the theory of Stark broadening in a plasma is introduced and the influence of the Zeeman splitting and Doppler broadening on the Stark broadened line shapes is investigated. The spectroscopic setup and the way in which the density is evaluated will be presented in Section 3. Initial density measurements are compared with other diagnostics as a validation check in Section 4 and conclusions are given in Section 5.

## 2. Theory of Stark broadening in a plasma

We focus here on hydrogen or a hydrogen isotope as the emitting atom and on the Balmer transitions as they emit in the visible spectral range. The broadening effect is proportional to the density of the surrounding particles and can, therefore, be used as a measure of this parameter if the relationship between particle density and spectral line shape is known. As the surrounding particles in a plasma are charged particles, this special type of pressure broadening is called *Stark broadening*. There is, in first order, a division into two extreme approximations, i.e. the collision broadening (also called *impact theory*) and the quasi-static broadening (*statistical theory*) [4]. The impact theory is valid if the duration of the perturbation, $t_p \approx r/v_{rel}$ with the distance $r$ between the emitting atom and the disturbing plasma particle and their relative velocity $v_{rel}$, is short compared to the time of interest, $\tau_i$, which is the inverse of the frequency shift caused by the perturbation. This collision broadening determines the line shape in the central part of the broadened spectral line. On the other hand, if the perturbers move relatively slowly, then the perturbation is constant over $\tau_i$ and the statistical theory is valid. Here, the statistically distributed perturbers produce electric fields which lead to the Stark splitting. This mechanism determines the shape of the line wings. According to the value of $\tau_i/t_p$ one can define a critical wavelength shift $\Delta\lambda_c$ below which the collision damping theory can be used and above which the statistical theory applies [5]:

$$\Delta\lambda_c = \frac{\bar{v}_{rel}^2\,\lambda_0^2\,m_e}{3\,\pi^3\,\hbar\,c\,\overline{\Delta n_k}} \tag{1}$$

with the unperturbed wavelength $\lambda_0$, the electron mass $m_e$, the velocity of light $c$ and an average splitting of the transition lines $\overline{\Delta n_k}$ due to the linear Stark effect. For the Balmer lines $H_\beta$ ($n = 3 \rightarrow 2$) up to $H_\epsilon$ ($n = 7 \rightarrow 2$) on gets $\overline{\Delta n_k} = 5.97$; 11.82; 15.94; 24.59 [6]. Moreover, the critical wavelength shift is different for electrons and ions as it depends on the relative thermal velocity of the emitting atom and the disturbing particle. Table 1 shows $\Delta\lambda_c$, which has been calculated for different Balmer lines and temperatures.
It can be seen from this simple approximation that in the case of electrons $\Delta\lambda_c$ is very large, meaning that the impact theory can be used throughout the entire spectrum. For the ions, however, the statistical theory is valid, with an exception in the very center of the spectral line where the collision damping theory has to be applied. This exception

**Table 1.** Critical wavelength shift $\Delta\lambda_c$ for different Balmer lines and temperatures.

| Temperature: | | 5 eV | 10eV | 20 eV |
|---|---|---|---|---|
| $D_\beta$ | Electrons | 73.23 nm | 146.4 nm | 292.9 nm |
| | Ions | 0.040 nm | 0.060 nm | 0.100 nm |
| $D_\gamma$ | Electrons | 21.94 nm | 43.88 nm | 87.75 nm |
| | Ions | 0.012 nm | 0.018 nm | 0.030 nm |
| $D_\delta$ | Electrons | 9.90 nm | 19.79 nm | 39.58 nm |
| | Ions | 0.005 nm | 0.008 nm | 0.013 nm |
| $D_\epsilon$ | Electrons | 6.88 nm | 13.76 nm | 27.52 nm |
| | Ions | 0.004 nm | 0.006 nm | 0.009 nm |

becomes less important for the higher members of the Balmer series.

Besides numerical simulations [7] an analytical unified description of the electrons and ions can be done with the *model microfield method* (MMM), derived by Brissaud and Frisch [8]. Here, time dependent electric micro fields produced by the plasma electrons and ions are introduced, where the field strength jumps instantaneously between constant values in a stochastic way [9, 10]. The jump frequency is chosen so as to allow for a correct description of both, the Stark splitting (statistical theory) and the collision broadening [11]. In addition, through the superposition of two stochastically independent processes, a unified description of the electron and ion perturbation is possible. Based on the MMM, Stehlé and Hutcheon have calculated and published Stark broadened spectral lines for several members of the Lyman and Balmer series for a wide density and temperature range [12, 13]. At present these profiles are one of the most accurate ones with an uncertainty better than 10% and widely accepted. However, these tables cannot be simply adopted to magnetically confined fusion plasmas as the influence of the additional magnetic field on the Stark broadened line shape via Zeeman splitting is not included. There exist tables including the Zeeman splitting [14] but only for the $D_\alpha$ and $D_\beta$ lines. However, we want to use the higher series members which will be discussed later.

We have calculated Stark broadened line shapes using the *unified theory* [4, 15] which does not retain ion dynamics and compared them to the MMM profiles to illustrate the effect of the ion dynamics. The semi quantum mechanical unified theory is an extension of the impact theory [16] including incomplete electron collisions. With the unified theory it is possible to combine the collision broadening by electrons with the Stark splitting (statistical theory) caused by the ions. In the Schrödinger equation the electron contribution is described with a collision operator [17] and the ion contribution via an interaction Hamiltonian $H = e\,\vec{r}\cdot\vec{E}$ (linear Stark effect). For the electric field strengths produced by the ions we used the Mozer–Baranger distribution function [18, 19], which is based on the Holtsmark distribution function [20] and additionally accounts for Debye shielding and ion–ion interactions. It should be noted here that the

distribution function derived by Hooper [21, 22] is similar to the one by Mozer–Baranger for our plasma conditions. As the ion broadening is calculated via the static theory, it is not possible to include the collision broadening due to the ions, valid in the very center of the line (see Tab. 1).

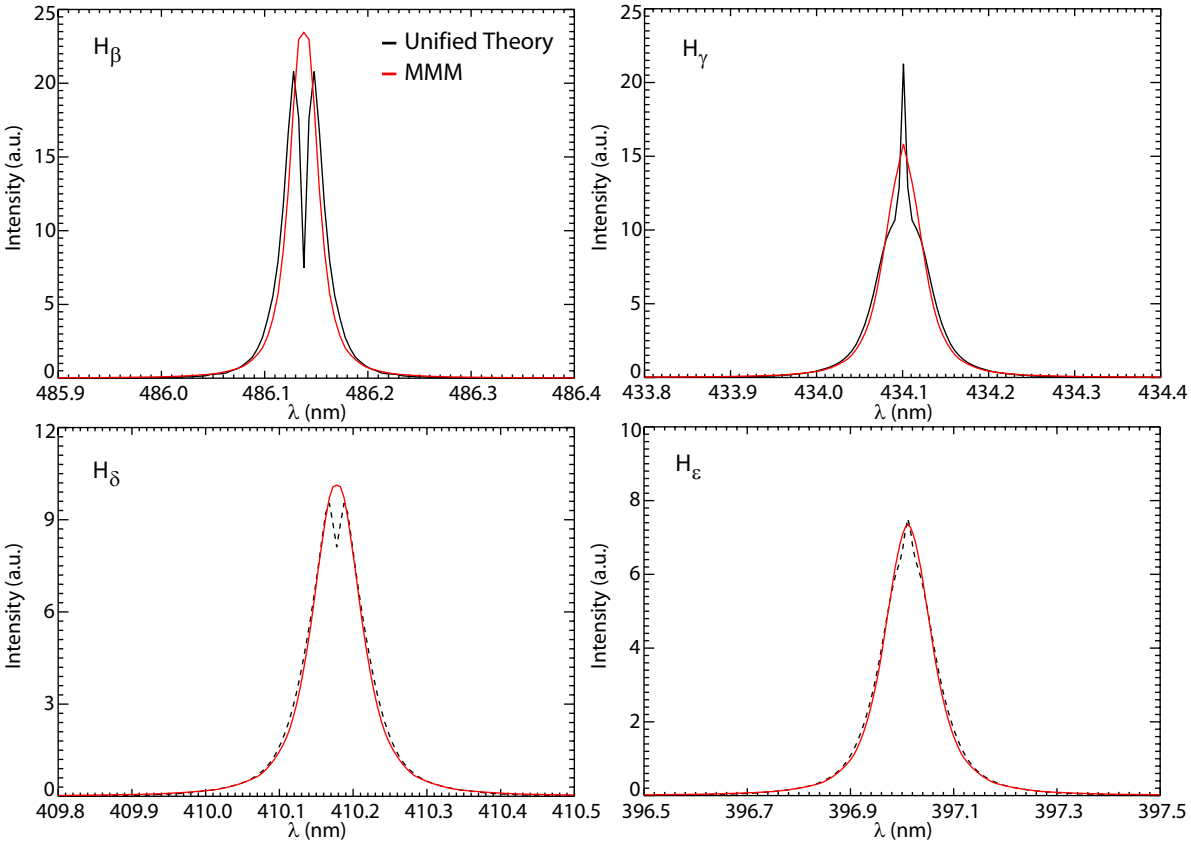


**Figure 1.** Stark profile of $n_e = 1 \cdot 10^{20}\,\mathrm{m}^{-3}$ and $T_e = 10\,\mathrm{eV}$ for different Balmer lines calculated with the unified theory compared to the MMM profiles published by Stehlé [13].

We have calculated the Stark broadened profiles based on the unified theory for different Balmer lines and a typical density in the AUG divertor of $1 \cdot 10^{20}\,\mathrm{m}^{-3}$. Figure 1 compares these profiles with the according profiles published by Stehlé and Hutcheon based on the MMM. The $\propto \Delta\lambda^{-5/2}$ decay of the Stark broadened line wings, which results from the Holtsmark distribution function, is clearly visible for the high–n Balmer lines and is a well known observation. Moreover, the unified theory profiles have narrower line centers due to the missing ion collision broadening, which leads to broader line wings. In agreement with Table 1 this effect becomes less important with higher upper principal quantum number. Considering further that the line center is smeared out by folding the Stark profile with an additional Doppler profile and the instrument function (sec. 3.2), the difference between the two theories becomes negligible for the higher members of the Balmer series. This implies that we can use the unified theory to investigate an additional Zeeman splitting on the Stark broadened line shapes.

Stark and Zeeman broadened profiles by introducing another interaction Hamiltonian which accounts for the Zeeman splitting have been already calculated by Mathys for $H_\alpha$ [23] based on the unified theory and by Nguyen-Hoe for $H_\alpha$ and $H_\beta$ [17] based on the impact theory. Measuring the higher Balmer series members is practically beneficial as the Stark broadening becomes stronger with higher upper principal quantum numbers (see Fig. 1). Therefore we extended the calculations by Nguyen-Hoe to $H_\gamma$ up to $H_\epsilon$. Figure 2 compares for the Balmer lines $H_\beta$ up to $H_\epsilon$ and $n_e = 1 \cdot 10^{20}\,\mathrm{m}^{-3}$ calculated Stark profiles based on the impact theory with and without a typical AUG magnetic field of $B = 2.5\,\mathrm{T}$. It can be seen that the influence of the Zeeman splitting on the line broadening can be neglected for the higher members of the Balmer series. It should be noted here again that the line center is smeared out by the convolution with an additional Doppler profile and the instrument function.

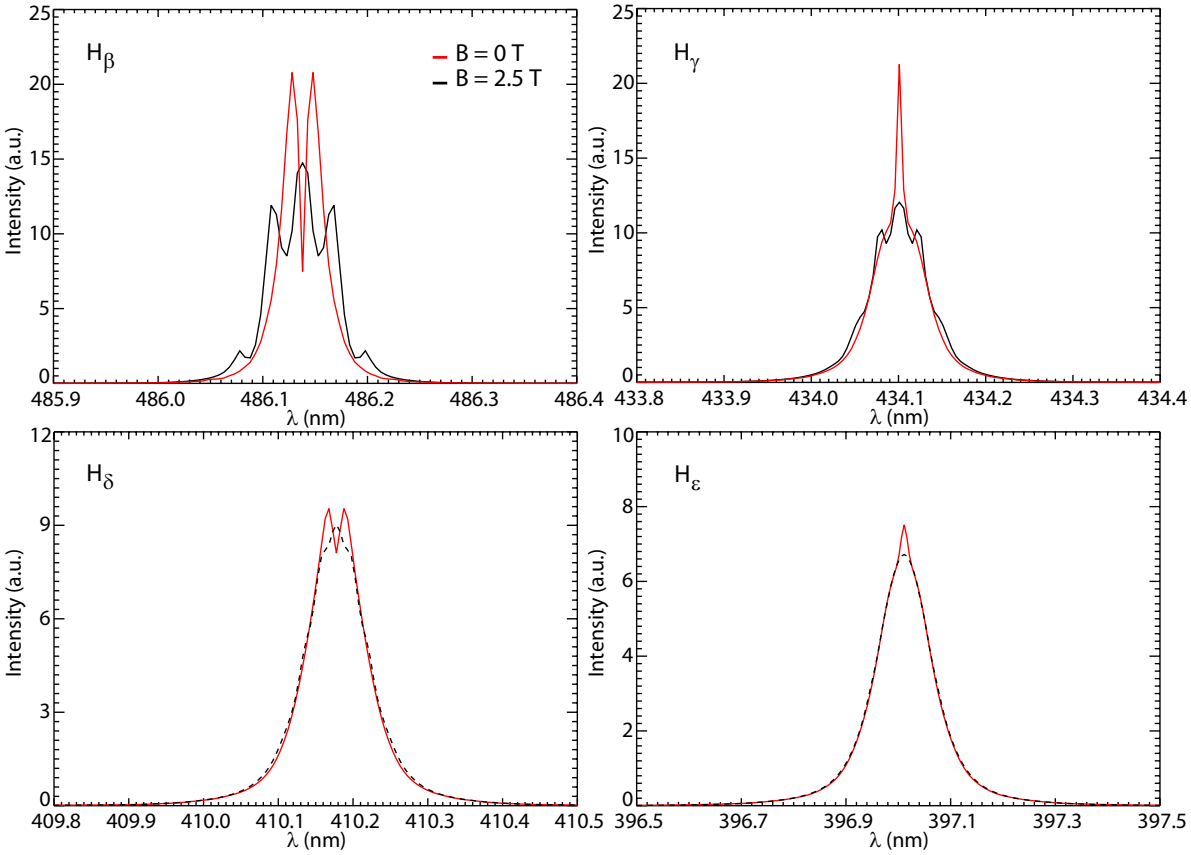


**Figure 2.** Stark profiles of $n_e = 1 \cdot 10^{20}\,\mathrm{m}^{-3}$ and $T_e = 10\,\mathrm{eV}$ for different Balmer lines calculated with the impact theory with and without an additional magnetic field of $B = 2.5\,\mathrm{T}$.

The Doppler broadening is caused by the thermal motion of the emitting neutral particles with temperature $T_n$. In a thermal equilibrium the velocity distribution is a Maxwellian, which results in a Gaussian line shape. In order to be able to evaluate $n_e$ from the Stark broadening we are constrained to a fixed Doppler broadening. Therefore, $T_n = 5\,\mathrm{eV}$ is assumed, which is the maximum Franck-Condon dissociation energy of

recycled $H_2$ molecules. The Doppler broadening mainly influences the central part of the line, while the wings show still the pure Stark profile due to the weak $\Delta\lambda^{-5/2}$ decay. Nevertheless, in Figure 3 the FWHM of a Stark and Doppler broadened $D_\epsilon$ line is shown for various $n_e$ and $T_n$ values as an indication for the influence of the Doppler broadening on the Stark profile. For densities larger than $n_e \approx 4 \cdot 10^{19}\,\mathrm{m}^{-3}$ the FWHM is insensitive to small changes around $T_n = 5\,\mathrm{eV}$.

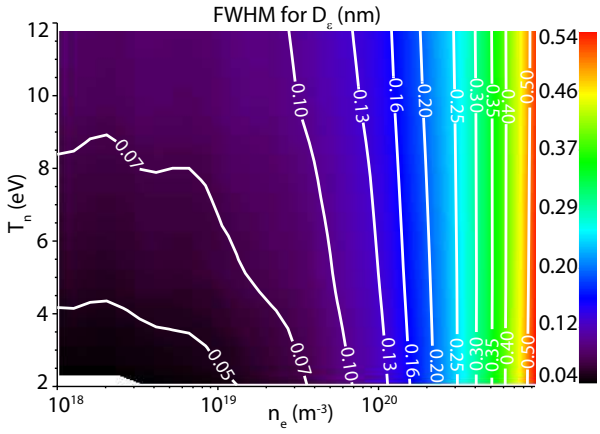


**Figure 3.** FWHM of a Stark and Doppler broadened $D_\epsilon$ line for different neutral temperatures and electron densities.

## 3. Diagnostic setup and data evaluation

### *3.1. Diagnostic setup*

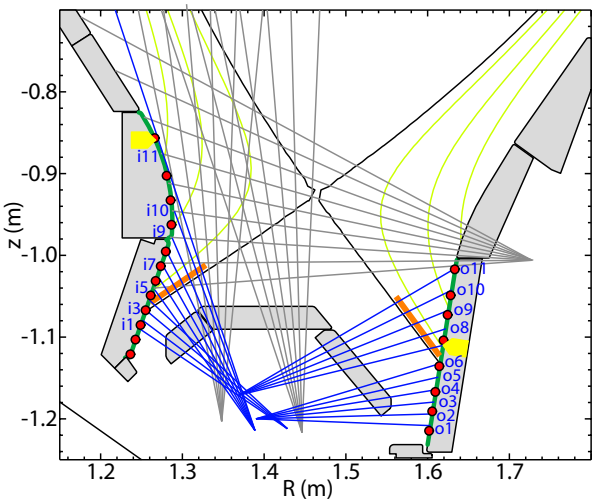


**Figure 4.** Geometry of the Stark diagnostic LOS (blue). Also shown are pressure gauges (yellow), Langmuir probes (red) and the $\Delta S$ coordinates (green). See text for more information.

Figure 4 shows the geometry of the spectroscopic lines of sight (LOS) in the divertor of AUG. During this work, only the blue LOS were available, which allow the determination of the electron density in the inner and outer divertor strike point region. The gray LOS have been recently installed to increase the spatial coverage in the divertor. The collected light is transmitted via silica optical fibers with a diameter of 400 $\mu$m to a Czerny Turner like spectrometer. The polished ends of the fibers are mounted directly in front of the entrance slit of the spectrometer. The light is then dispersed with a reflection grating of 2400 lines/mm and focused on an EM-CCD camera. The spectrometer is equipped with commercial camera lenses. The collimating lens has a focal length of 280 mm and a F-number of 4 while for the focusing lens these parameters are $f = 180$ mm and $F = 2.8$. The different focal lengths yield a de–magnification of 180/280 of the image on the CCD chip. The size of the CCD chip is 656 pixels in horizontal and 496 pixels in vertical direction with a pixel size of $7.4 \times 7.4\,\mu$m. The wavelength resolution is $\Delta\lambda = 0.07$ nm at 400 nm and the imaged wavelength range is about 9 nm. With vertical binning a simultaneous measurement of 11 LOS with an acquisition time of $\Delta t = 2.5$–3 ms can be achieved. When reading out just one LOS, the acquisition time can be decreased down to $\Delta t = 0.2$ ms. Furthermore the CCD camera is equipped with a 12 bit analog-to-digital converter. The entrance slit of the spectrometer is set to 50 $\mu$m, which is a good compromise between good wavelength resolution and the signal strength. This yields a rectangular-shaped instrument function with a width on the CCD chip of about 0.04 nm, shown in Figure 5.

### *3.2. Data evaluation*

As shown in Figure 1 the broadening of the Stark profiles becomes larger with higher upper principal quantum number. Measuring the higher members of the Balmer series therefore makes less demands on the spectral resolution of the spectrometer. As a compromise between high Balmer series member and a good signal to noise ratio, the $D_\delta$ or the $D_\epsilon$ line is used by default for the density evaluation.

Furthermore, it was shown that the Zeeman effect can be neglected when measuring the higher Balmer lines (Fig. 2). As the MMM profiles published by Stehlé [13] are widely accepted and, in the case of the higher Balmer lines, similar to the profiles obtained with the unified theory (Fig. 1), the MMM profiles are used and the Zeeman splitting is neglected.

Theoretic profiles of the Stark broadened Balmer line are calculated for 28 different densities in the wavelength range of interest between $1 \cdot 10^{19}\,\mathrm{m}^{-3} < n_e < 1 \cdot 10^{22}\,\mathrm{m}^{-3}$. These calculated profiles are then convoluted with the Doppler broadened Gaussian profile corresponding to $T_n = 5$ eV and the instrument function (Fig. 5). The profile of an arbitrary density value is obtained by a linear interpolation between these calculated profiles. When additional impurity lines appear within the spectrum they are also taken into account. They are modeled as a convolution of the Doppler profile with the instrument function only. All profiles are normalized to an intensity of 1. This

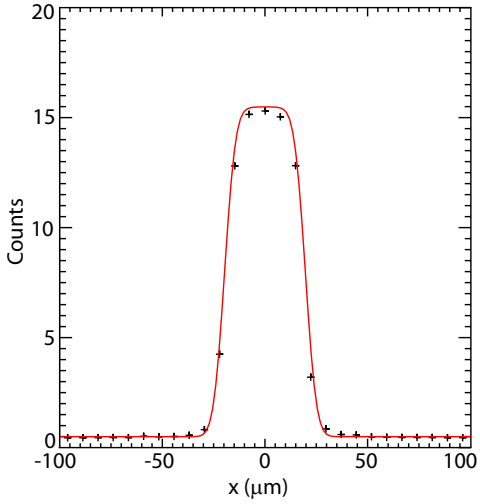


**Figure 5.** Instrument function for an entrance slit width of 50 $\mu$m

theoretic spectrum is then fitted to the measured data using a *least squares* method where $n_e$, as well as the intensities of the lines and the background radiance are fit parameters. Figure 6 shows an example of such a fit on the $D_\epsilon$ line. In addition to the Balmer line ($\lambda_{D_\epsilon} = 396.90\,\text{nm}$) there is a nitrogen line ($\lambda_{NI} = 395.59\,\text{nm}$), a helium line ($\lambda_{HeI} = 396.47\,\text{nm}$), an oxygen line ($\lambda_{OII} = 396.21\,\text{nm}$) and an oxygen multiplet ($\lambda_{OI} = 395.44\,\text{nm};\ 397.33\,\text{nm};\ 398.27\,\text{nm}$) within the regarded wavelength range. The $\Delta\lambda^{-5/2}$ decay of the $D_\epsilon$ line, which is characteristic for the Stark broadening (Fig. 1), can bee clearly seen in Figure 6. The fact that most of the information about $n_e$ is in the Stark broadened lines wings favors the fitting of the entire profile compared to measuring just the FWHM. In addition, fitting of the whole profile is more robust and gives more accurate and reliable results.

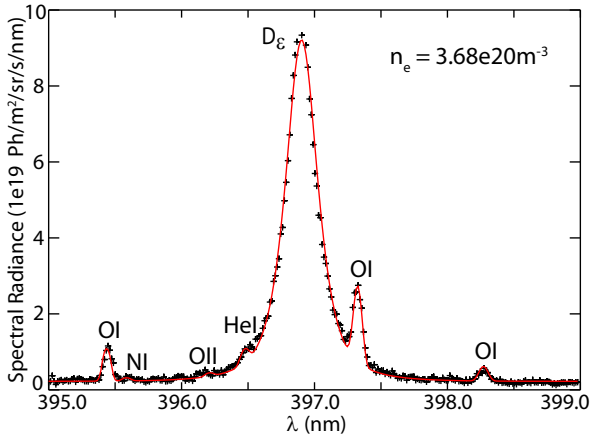


**Figure 6.** Example fit to the $D_\epsilon$ line yielding $n_e$.

Stehlé and Hutcheon claim an uncertainty better than 10% in their profiles, where quasi–neutrality is assumed, i.e. $n_e = n_i$. In AUG, the typical effective charge is about 1.2, which imposes an additional uncertainty. This effect was discussed e.g. in Ref.

[24]. Therefore, we expect an uncertainty of this measurement of about 15%. One can consider applying a forward model to simulate the line shapes, where such factors like impurity profiles along a LOS or non–Maxwellian distribution of plasma parameters can be included. But this would strongly increase the computational time and is beyond the scope of this diagnostic. With the current setup, we can provide density measurements for 11 LOS and 3500 time frames on a inter–shot basis of about 20 minutes.

The lower measurement range of this diagnostic is set by two constraints. On the one hand, as shown in Fig 3, at densities below $n_e \approx 4 \cdot 10^{19}\,\mathrm{m}^{-3}$ the Doppler profile becomes comparable to the Stark profile. Thus this is the lowest measurable density. On the other hand the divertor must be in the medium to high recycling regime to obtain a reasonable signal to noise ratio of the higher Balmer lines. Finally, it should be noted that, although this is a measurement along a line of sight, the density measurement is localized to regions where the $D_\epsilon$ emissivity is highest. Furthermore, as the measured profile is a convolution of the local Stark broadened profiles weighted by the local $D_\epsilon$ emissivity, the density which is measured is not an average density but close to the maximum density along the LOS.

### *3.3. Reflection issue*

Since 2007 the plasma facing surfaces of AUG have been completely covered with Tungsten [25], which has a high reflectivity not only for complete but also for diffusive reflection ($R_{tot} \approx 35 - 40\%$, [26]). This seriously disturbed the initial attempts to measure the Balmer lines. Under normal operation the density as well as the radiance of the Balmer line is about one order of magnitude higher in the inner divertor than in the outer divertor (see section 4.3). This caused the LOS observing the outer divertor mainly to detect the radiance originating from the inner divertor that was reflected off of the outer target. Therefore a much too high $n_e$ was determined in the outer divertor. To address this problem, the LOS in the outer divertor were rearranged such that they end in a $\approx 6\,\mathrm{mm}$ wide viewing dump between two tiles. This strongly reduces the detection of stray radiation. To document this enhancement a discharge in which $n_e$ was determined with the old LOS setup was repeated with the new LOS setup. Figure 7 shows a comparison of an example fit to the $D_\epsilon$ line measured with the new and old LOS setups. It can be seen that the radiance of $D_\epsilon$ as well as the resulting density is considerably lower with the new LOS setup.

## 4. Consistency check

In this section we present initial measurements and show that the obtained $n_e$ values are self consistent as well as consistent with other diagnostics.

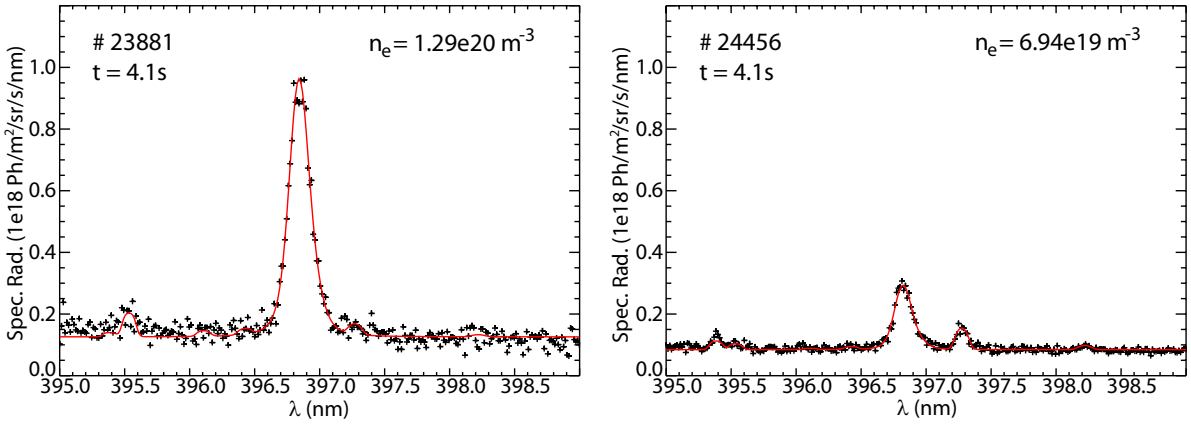


**Figure 7.** Fit to the $D_\epsilon$ line measured with the old (left) and new (right) LOS setup for two identical discharges.

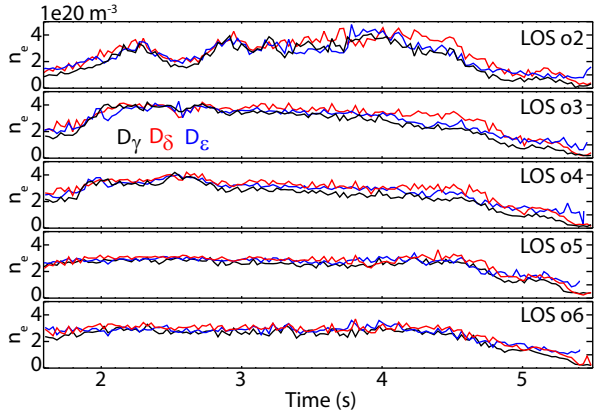


**Figure 8.** Time traces of the electron density obtained with the $D_\gamma$ (black), $D_\delta$ (red) and $D_\epsilon$ line (blue) for various LOS

### *4.1. Consistency of obtained $n_e$ using different Balmer lines*

As discussed in section 3.2 the $D_\delta$ or $D_\epsilon$ line is used by default for the $n_e$ evaluation. Here we show that the usage of different Balmer lines yields similar results. To do this we measured the $D_\gamma$, $D_\delta$ and $D_\epsilon$ lines successively in three separate but similar discharges. The density obtained for different Balmer lines, measured by five LOS in the outer divertor (see Fig. 4), is shown in figure 8. It can be seen that the $n_e$ values for a given LOS obtained with the different Balmer lines are the same within 15 %.

### *4.2. ELM resolved measurement*

A feature that is associated with the H-Mode regime is the occurrence of edge localized modes (ELMs), which repetitively expel energy and particles from the plasma. These energy and particle bursts can be detected in the divertor. For example, there is a strong increase of the sputtered tungsten from the divertor target caused by such bursts. The lower plot in Figure 9 shows a spectroscopic measurement of the radiance of a WI line

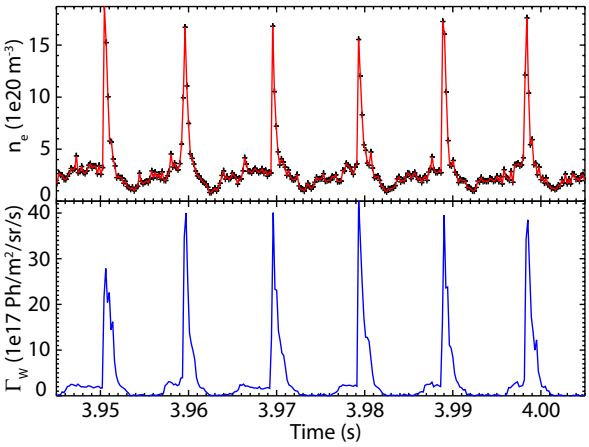


**Figure 9.** Time traces of $n_e$ from Stark broadening (red) and WI radiance (blue) in the outer divertor during several ELM cycles

at $\lambda_W = 400.8\,\mathrm{nm}$ in the outer divertor. The spikes in the signal are markers for the occurrence of an ELM. When measuring with only one LOS an acquisition time of $\Delta t = 0.2\,\mathrm{ms}$ can be achieved with the Stark diagnostic (section 3.1). This is sufficient for an ELM resolved determination of $n_e$. The temporal evolution of the density, shown in the upper plot of figure 9, is very well correlated with the tungsten radiance. In addition, during an ELM the electron density in the divertor is increased by a factor of $\approx 5$ and requires $1 - 2\,\mathrm{ms}$ to return to its equilibrium density.

### *4.3. Comparison with Langmuir probes*

The divertor of AUG is equipped with an extensive set of static Langmuir probes (LP), see Figure 4, which are used to measure $n_e$ and $T_e$ at the target. Here, $n_e$ obtained from the Stark broadening diagnostic (SBD) is compared with $n_e$ from LP. For this purpose a lower single null L-mode discharge with lower triangularity $\delta = 0.36$ was performed. It had a plasma current of $I_p = 0.8\,\mathrm{MA}$, a toroidal magnetic field of $B_t = -2.5\,\mathrm{T}$, a line averaged core plasma density of $\bar{n}_e = 4.5 \cdot 10^{19}\,\mathrm{m}^{-3}$, an additional heating power of $1.4\,\mathrm{MW}$ and a safety factor of $q_{95} \approx 5$. During this discharge strike point sweeps were performed to enhance the spatial resolution of the SBD and LP measurements. The outer divertor was in the medium recycling, conduction limited regime as the target temperature was $T_e \approx 20\,\mathrm{eV}$. The temperature at the inner divertor target was below $\approx 2\,\mathrm{eV}$ and thus, the inner divertor was in the detached regime. This can also be seen in the total radiation distribution (Fig. 10), which is derived from a tomographic reconstruction of foil bolometer measurements. The radiation front in the inner divertor, which is approximately the recycling front, has moved to the X-point, which indicates that the plasma is detached from the inner target.

In Figure 10 $n_e$ from SBD and LP as well as the radiance of the $D_\epsilon$ line versus the $\Delta S$ coordinate is shown for a time interval of $2.5\,\mathrm{s}$. Each symbol corresponds to the mean value of $\Delta t = 100\,\mathrm{ms}$. The $\Delta S$ coordinate is the poloidal distance from the strike

point along the divertor surface (Fig. 4). Positive values are in the scrape-off-layer (SOL) negative values are in the private flux region (PF). It must be noted here that the intersection of the LOS and the target is taken as the LOS position. The correct coordinate of the LOS would be the position where the $D_\epsilon$ emission along the LOS is highest, which is unknown, however. As the radiation is emitted somewhere in the SOL between the separatrix and the divertor target, the correct LOS coordinate is between the $\Delta S$ coordinate along the divertor surface and the distance from the strike point along the separatrix (orange lines in Fig. 4).

In the outer divertor a good agreement is obtained between $n_e$ at the strike point from SBD and LP, see Figure 10a. The fact that the shapes of the density profiles do not match is caused by the line integrated SBD measurement discussed above. The hydrogen ionization rate coefficient for $T_e = 20\,\mathrm{eV}$ and $n_e = 4 \cdot 10^{19}\,\mathrm{m}^{-3}$ is $\langle \sigma v_e \rangle = 2.2 \cdot 10^{-14}\,\mathrm{m}^3/\mathrm{s}$ and has been taken from ADAS [27] based on a Collisional Radiative Model [28]. With a temperature of the neutral deuterium of $T_n = 5\,\mathrm{eV}$ the mean free path of neutrals is approximately $\lambda_{mfp} \approx 3.5\,\mathrm{cm}$. Thus, the region where the recycled neutrals ionize expands from the divertor target into the SOL along a narrow region close to the separatrix where the temperature is highest (orange line in Fig. 4). The SBD measures therefore the density distribution approximately along the separatrix into the divertor volume and not along the divertor target plate. The $\approx 7\,\mathrm{cm}$ broad profile along the target (Fig. 10a) corresponds to a $\approx 5\,\mathrm{cm}$ wide region along the separatrix, which is of the order of $\lambda_{mfp}$. Therefore, the density profile along the separatrix is expected to be flat in this narrow region close to the target, as observed by the SBD. The Langmuir probes, in contrast, measure the density at the target and yield a decay of the density profile outside of the ionization front. The SBD diagnostic can therefore be used to determine the density distribution in the divertor volume.

In the detached inner divertor there is no agreement between $n_e$ from SBD and LP (Fig. 10c). In fact, the peak $n_e$ measured by SBD of $\approx 2.3 \cdot 10^{20}\,\mathrm{m}^{-3}$ is about two orders of magnitude higher than $n_e$ from LP at the target and about one order of magnitude higher than the core plasma density. This result is expected as in detached conditions the pressure and hence $n_e$ in front of the target reaches very low values [29]. The region of highest $n_e$ is retracted from the target and in the divertor volume, which is also confirmed by the distribution of the total radiation (Fig. 10e). Moreover, high values for $n_e$ in a detached divertor volume, which are one order of magnitude higher than the core plasma density, have also been observed at other devices [30, 1, 31].

### *4.4. Comparison with pressure gauges*

Finally, SBD measurements are compared to measurements from fast ionization gauges (ION). These gauges measure the neutral flux density $\Gamma_{D^0}$ [32] at different positions. The gauges of interest are shown in Figure 4. In attached conditions, $\Gamma_{D^0}$ at the divertor target can also be derived from the SBD measurements with the so-called S/XB method [33]:

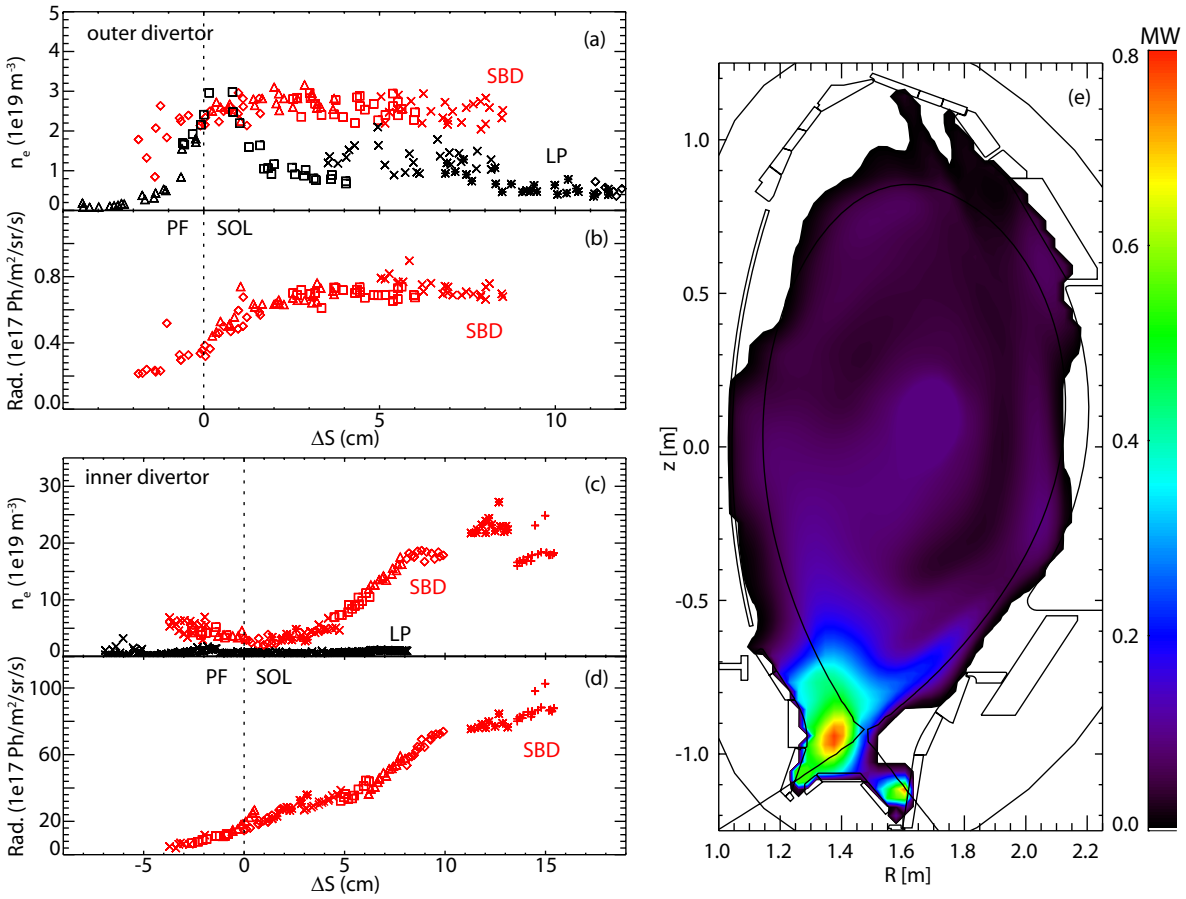


**Figure 10.** Profiles of (a,c) $n_e$ measured by SBD (red) and LP (black) and (b,d) $D_\epsilon$ radiance for the outer and inner divertor, respectively. The different symbols indicate different LOS and probes. (e) Total radiation distribution measured by foil bolometers of discharge # 24456.

$$\Gamma_{D^0} = \frac{S}{XB}\Gamma_\gamma \tag{2}$$

The neutral flux is the photon flux, $\Gamma_\gamma$, multiplied with the ratio of the rate coefficient for ionization, $S$, to the rate coefficient for excitation, $X$, times the branching ratio, $B$. The photon flux is derived by projecting the measured Balmer emission along the LOS (shown in Fig. 10b,d) onto the surface normal and multiplying it by $4\pi$, which accounts for homogeneous emission in the full solid angle. The $S/XB$ value is a function of $n_e$ and $T_e$ and is taken from ADAS. In [34] neutral fluxes have been calculated based on a spectroscopic $D_\alpha$ measurement and compared to the gauge measurements. For the $S/XB$ value $T_e$ and $n_e$ have been taken from LP. One restriction of the S/XB method is that ionization processes must dominate with respect to recombination, which is fulfilled in attached but not in detached divertor conditions where recombination processes are dominant. Therefore, good agreement between both flux measurements was derived in attached conditions, but in detached conditions the spectroscopic neutral fluxes were

$\approx$ 3 times larger than the fluxes measured by the pressure gauges [34]. In this work, we use the $D_\epsilon$ line and for the $S/XB$ value $T_e$ and $n_e$ are taken from LP and SBD, respectively.

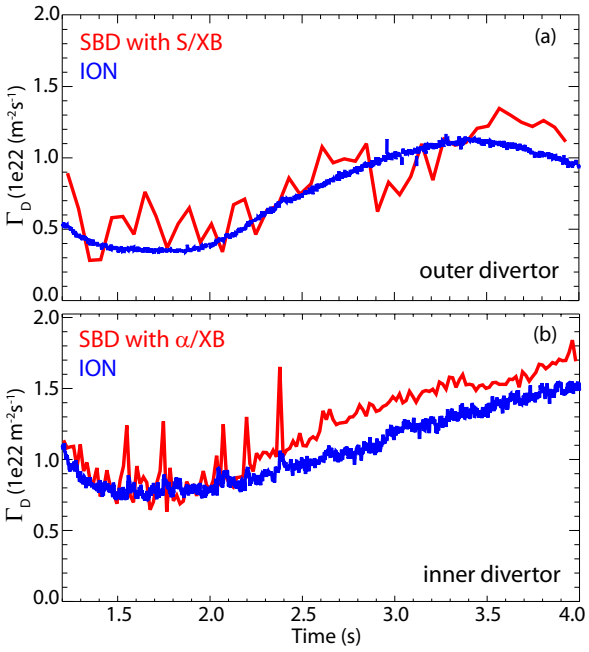


**Figure 11.** Time traces of $\Gamma_{D^0}$ measured by ionization gauges and calculated from SBD measurements for the inner (a) and outer (b) divertor of discharge # 24456.

In Figure 11a $\Gamma_{D^0}$ measured by the outer divertor ionization gauge and calculated with the S/XB method for the LOS closest to this gauge (*o7*, Fig. 4) are shown. There is a good agreement between both flux densities, which shows that the density and the $D_\epsilon$ emission measured by the SBD, in combination with $T_e$ from LP, are consistent with the ionization gauge measurement.

The inner divertor is in the detached regime, as discussed in the previous section. As a consequence, recombination processes now dominate with respect to ionization. In order to calculate the neutral flux from the SBD measurement, we exchange the rate coefficient for ionization, $S$, in equation 2 with the according rate coefficient for recombination, $\alpha$, which is also taken from ADAS. For the rate coefficients $n_e$ and $T_e$ are taken again from SBD and LP, respectively. Figure 11b compares $\Gamma_{D^0}$ calculated from the SBD measurement (*i11*, Fig. 4) with the one measured by the ionization gauge. Both fluxes agree reasonably well within the uncertainties of $\approx$ 20 %. Taking for the $\alpha/XB$ value the density measured by LP, which is more than one order of magnitude lower than the one from SBD (Fig. 10), results in a $\approx 3-4$ times lower $\Gamma_{D^0}$. This reveals that also in detached conditions the SBD measurements are consistent with the ionization gauge measurement and that neutral deuterium fluxes can be determined via spectroscopy, provided that the electron density in the divertor volume is known.

## 5. Conclusion

A new diagnostic capable of measuring the electron density in the divertor volume has been successfully installed in AUG. The diagnostic is based on a spectroscopic measurement of the Stark broadening of the Balmer lines. It has been shown that both, the model microfield method (MMM) and the unified theory, where the ion dynamics is missing, yield similar Stark profiles for the Balmer lines with higher upper principal quantum number $n$. The influence of the Zeeman splitting on the Stark profile was investigated by calculating the corresponding line shapes via the unified theory. It was found that the Zeeman splitting can be neglected for the high $n$ Balmer lines and typical AUG magnetic fields of $\approx 2.5\,\mathrm{T}$. In contrast, the Doppler broadening has to be taken into account, where a fixed neutral temperature of 5 eV, which is the maximum Franck-Condon dissociation energy of recycled $H_2$ molecules, was found to be sufficient.

In summary, MMM Stark profiles, convoluted with a fixed Doppler broadening and with the instrument function are fitted to the measured $D_\delta$ or $D_\epsilon$ line, yielding $n_e$ and the radiance of the Balmer line. The fact that most of the information about $n_e$ is in the Stark broadened line wings, as they decay $\propto \Delta\lambda^{-5/2}$, favors the fitting of the entire profile compared to measuring just the FWHM. The uncertainty of this measurement is about 15% and the lower measurement range is $n_e \approx 4 \cdot 10^{19}\mathrm{m}^{-3}$.

Initial $n_e$ measurements has been successfully compared to other diagnostics as a validation check on the method. In attached conditions, good agreement with Langmuir probes (LP) has been obtained. Neutral fluxes, calculated from the $D_\epsilon$ radiance and $n_e$ from the Stark broadening diagnostic (SBD) and $T_e$ from LP, are in good agreement with neutral fluxes from pressure gauges for both, attached and detached divertor conditions. Here, neutral fluxes in detached, recombination dominated conditions have been derived from spectroscopy for the first time, owing to the knowledge of the density in the divertor volume which is not accessible for LPs. Studying this density distribution in the detached divertor volume will be the main focus of this new diagnostic.

## References

[1] B. Lipschultz, B. LaBombard, J.L. Terry, C. Boswell, and I.H. Hutchinson. Divertor physics research on Alcator C-Mod. *Fusion Science And Technology*, 51(3):369–389, 2007.

[2] A.G. Meigs, G.M. McCracken, C. Maggi, R.D. Monk, L.D. Horton, M. von Hellermann, M.F. Stamp, and P. Breger. Spectroscopic electron density measurements and evidence of recombination in high density JET divertor discharges. In *Europhysics Conference Abstracts (Proc. of the 25th EPS Conference on Plasma Physics, Prague, Czech Republic, 1998)*, pages P–1.017. European Physical Society, 1998.

[3] R.D. Bengston, J.D. Tannich, and P. Kepple. Comparison between measured and theoretical Stark-Broadened profiles of $H_6$-$H_{12}$ emitted from a low density plasma. *Phys. Lett. A*, 1:532–533, 1970.

[4] H.R. Griem. *Plasma Spectroscopy.* McGraw-Hill Book Company, 1997.

[5] T. Holstein. Pressure broadening of spectral lines. *Phys. Rev.*, 79:744, 1950.

[6] A. Unsöld. *Physik der Sternatmosphären.* Springer-Verlag, 1955.

[7] E. Stambulchik and Y. Maron. Plasma line broadening and computer simulations: A mini-review. *High Energy Density Physics*, 6(1):9 – 14, 2010.

[8] A. Brissaud and U. Frisch. Theory of Stark broadening II - exact line profile with Model Microfield. *J. Quant. Spectrosc. Radiat. Transfer*, 11:1767–1783, 1971.

[9] J. Seidel. Hydrogen stark broadening by different kinds of Model Microfields. *Z. Naturforsch.*, 35a:679–689, 1980.

[10] A. Brissaud and U. Frisch. Solving linear stochastic differential equations. *J. Math. Phys.*, 15:524–534, 1974.

[11] A. Brissaud, C. Goldbach, L. Leorat, A. Mazure, and G. Nollez. On the validity of the Model Microfield Method as applied to Stark broadening of neutral lines. *J. Phys. B: At. Mol. Phys.*, 9:1147–1162, 1976.

[12] C. Stehlé. Stark broadening of hydrogen Lyman and Balmer in the conditions of stellar envelopes. *Astron. Astrophys. SuppL. Ser.*, 104:509–527, 1994.

[13] C. Stehlé and R. Hutcheon. Extensive tabulations of Stark broadened hydrogen line profiles. *Astron. Astrophys. SuppL. Ser.*, 140:93–97, 1999.

[14] S. Günter and A. Könies. Diagnostics of dense plasmas from the profile of hydrogen spectral lines in the presence of a magnetic field. *J. Quant. Spectrosc. Radiat. Transfer*, 62:425–431, 1999.

[15] C.R. Vidal, J. Cooper, and E.W.Smith. Unified theory calculations of Stark broadened hydrogen lines including lower state interactions. *J. Quant. Spectrosc. Radiat. Transfer*, 11:263–281, 1971.

[16] H.R. Griem, A.C. Kolb, and K.Y. Shen. Stark broadening of hydrogen lines in a plasma. *Phys. Rev.*, 116:4–16, 1959.

[17] Nguyen-Hoe, H.W. Drawin, and L. Herman. Effet d'un champ magnetique uniforme sur les profiles des raies de l'hydrogene. *J. Quant. Spectrosc. Radiat. Transfer*, 7:429–474, 1967.

[18] B. Mozer and M. Baranger. Electric field distribution in an ionized gas I. *Physical Review*, 115:521–531, 1959.

[19] B. Mozer and M. Baranger. Electric field distribution in an ionized gas II. *Physical Review*, 118:626–631, 1960.

[20] J. Holtsmark. Über die Verbreiterung von Spektrallinien. *Annalen der Physik*, 58:577–630, 1919.

[21] C.F. Hooper. Electric microfield distributions in plasmas. *Phys. Rev.*, 149:77–91, 1966.

[22] C.F. Hooper. Low-frequency component electric microfield distributions in plasmas. *Phys. Rev.*, 165:215–222, 1968.

[23] G. Mathys. Hydrogen lines Stark broadening tables in the presence of a magnetic field. *Astron. Astrophys. SuppL. Ser.*, 59:229–253, 1985.

[24] J. Halenka, W. Olchawa, B. Grabowski, and F. Gajda. Perturber's charge effect on Stark broadened hydrogen lines in helium plasmas. *J. Quant. Spectrosc. Radiat. Transfer*, 74(5):539 – 544, 2002.

[25] R Neu, V Bobkov, R Dux, J C Fuchs, O Gruber, A Herrmann, A Kallenbach, H Maier, M Mayer, T Pütterich, V Rohde, A C C Sips, J Stober, K Sugiyama, and ASDEX Upgrade Team. Ten years of W programme in ASDEX Upgrade - challenges and conclusions. *Phys. Scr.*, T138:014038 (6pp), 2009.

[26] J. Harhausen, A. Kallenbach, C. Fuchs, and ASDEX Upgrade Team. Interpretation of $D_\alpha$ video diagnostics data as a contribution to plasma edge characterization. *Plasma Phys. Control. Fusion*, 53:025002–, 2011.

[27] H.P. Summers. ADAS User Manual 2.6. *http://www.adas.ac.uk./manual.php*, 2004.

[28] H.P. Summers, W.J. Dickson, M.G. O'Mullane, N.R. Badnell, A.D. Whiteford, D.H. Brooks, J. Lang, S.D. Loch, and D.C. Griffin. Ionization state, excited populations and emission of impurities in dynamic finite density plasmas: I. The generalized collisional-radiative model for light elements. *Plasma Phys. Control. Fusion*, 48(2):263, 2006.

[29] P.C. Stangeby. *The Plasma Boundary of Magnetic Fusion Devices.* Institute of Physics Publishing Bristol and Philadelphia, 2000.

[30] G.M. McCracken, R.D. Monk, A. Meigs, L. Horton, L.C. Ingesson, J. Lingertat, G.F. Matthews,

M.G. O'Mullane, R. Prentice, M.F. Stamp, and P.C. Stangeby. Volume recombination and detachment in JET divertor plasmas. *J. Nucl. Mater.*, 266–269:37–43, 1999.

[31] K. Fujimoto, T. Nakano, H. Kubo, K. Sawada, T.Takizuka, H. Kawashima, K. Shimizu, and N. Asakura. Spatial structure of volume recombination in JT-60U detached divertor plasmas. *Plasma Fusion Res.*, 4:025, 2009.

[32] A. Scarabosio and G. Haas. Behaviour of the ASDEX pressure gauge at high neutral gas pressure and applications for ITER. *AIP Conference Proceedings*, 988(1):238–242, 2008.

[33] K. Behringer, H. P. Summers, B. Denne, M. Forrest, and M. Stamp. Spectroscopic determination of impurity influx from localized surfaces. *Plasma Phys. Control. Fusion*, 31:2059–2099, 1989.

[34] A. Scarabosio, G. Haas, H. W. Müller, R. Pugno, M. Wischmeier, and ASDEX Upgrade Team. Measurements of neutral gas fluxes under different plasma and divertor regimes in ASDEX Upgrade. *J. Nucl. Mater.*, 390–391:494–497, 2009.